Front. Struct. Civ. Eng. 2021, 15(5): 1128–1143
https://doi.org/10.1007/s11709-021-0753-5

RESEARCH ARTICLE

Seismic response of precast reinforced concrete wall subjected to cyclic in-plane and constant out-of-plane loading

Shubham SINGHAL[a,b], Ajay CHOURASIA[a,b*], Soraj Kumar PANIGRAHI[a,b], Yogesh KAJALE[c]

[a] *Council of Scientific and Industrial Research, Central Building Research Institute, Roorkee 247667, India*
[b] *Academy of Scientific and Innovative Research (AcSIR), Ghaziabad 201002, India*
[c] *BG Shirke Construction Technology Pvt. Ltd., Pune 411036, India*
[*] *Corresponding author. E-mail: ajayc@cbri.res.in*

ABSTRACT This paper provides insight into the seismic behavior of a full-scale precast reinforced concrete wall under in-plane cyclic loading combined with out-of-plane loading replicated by sand backfill to simulate the actual condition of basement walls. The tested wall exhibited flexural cracks, owing to the high aspect ratio and considerable out-of-plane movement due to lateral pressure from the backfill. The wall performed satisfactorily by exhibiting competent seismic parameters and deformation characteristics governed by its ductile response in the nonlinear phase during the test with smaller residual drift. Numerical analysis was conducted to validate experimental findings, which complied with each other. The numerical model was used to conduct parametric studies to study the effect of backfill density and aspect ratio on seismic response of the proposed precast wall system. The in-plane capacity of walls reduced, while deformation characteristics were unaffected by the increase in backfill density. An increase in aspect ratio leads to a reduction in in-plane capacity and an increase in drift. Curves between the ratio of in-plane yield capacity and design shear load of walls are proposed for the backfill density, which may be adopted to determine the in-plane yield capacity of the basement walls based on their design shear.

KEYWORDS precast wall, basement wall, out-of-plane response, quasi-static test, sand backfill, seismic parameters

1 Introduction

Precast technology has a certain edge over conventional cast-*in situ* construction in terms of speed, quality, and construction efficiency [1]. The efficacy of precast reinforced concrete (RC) panels under gravity loads is well established [2], while their seismic behavior has been a subject of research for decades now. Some of the relevant recent studies on precast RC walls include that of Brunesi et al. [3], where precast RC wall-slab-wall type building system was subjected to monotonic and cyclic loading. Precast panels were connected with non-seismically designed steel connectors. The connection system failed in flexure, along with the total separation of precast panels [3]. Similar conclusions were drawn in another study [4] conducted on a similar system under dynamic loading on a shake table. The wall and slab components were connected through steel plates and mortar. The connection was the weakest link due to lack of shear transfer and damage in panel connectors, which resulted from the out-of-plane rocking of lateral walls [4]. Brunesi et al. [5] tested precast RC walls connected through steel hooks and bolts under lateral loading. Based on the results, a macro-model for fragility analysis was proposed for precast buildings. Other studies on the seismic behavior of precast walls include that of Singhal et al. [6,7], where precast walls were connected to precast columns through headed bars and loop bar connection, respectively. The literature revealed that the research on precast RC walls mainly relates to their seismic evaluation for application as a super-structural

Article history: Received Mar 19, 2021; Accepted Jun 14, 2021

component. However, literature on seismic behavior and application of precast RC structural walls as basement walls is scarce.

Basement RC walls behave distinctly compared to the structural walls in superstructure. Basement walls experience simultaneous out-of-plane and in-plane loading during earthquakes, which requires experimental investigation to ascertain their seismic response. Basement walls are typically designed as retaining walls for lateral pressure generated from the soil. 2010 Chile earthquake demonstrated brittle damage in basement RC walls due to combined bending and axial loading [8]. Additional seismic forces can be accounted for through a simplified pseudo-static approach or advanced dynamic analysis depending upon the time history acceleration of the earthquake. Commonly adopted methods for seismic analysis of basement retaining walls are Mononobe-Okabe (MO) method, Wood's method [9], and Steedman−Zeng method [10]. Although basement walls are restrained from bottom and top, they still tend to slide in in-plane direction or deflect in the out-of-plane direction, particularly during the seismic motion. To this consideration, basement walls cannot be considered as a rigid system, which otherwise may result in high design seismic earth pressure [11,12]. Alternatively, basement walls may be categorized as partially yielding walls [13].

Kalasin and Wood [14] proposed a macro-element model to predict the rotation and deformation of retaining walls under lateral earth pressure and ground acceleration. In another study, a cyclic test on reinforced soil retaining wall was conducted, and a relationship between vertical earth pressure and displacement was proposed [15]. Stability analysis of RC retaining wall subjected to seismic loading was performed to study the influence of friction angle of backfill, soil unit weight, and cohesion of soil [16]. Numerical empirical relations were developed for the seismic-resistant design of basement retaining walls based on stiffness degradation, damping, and soil conditions [13]. It has been reported that the current design practices of basement walls lead to over-conservative design. MO method is the most commonly adopted approach for analyzing retaining walls, which yields reasonably conservative results for seismic earth pressure [17,18]. Nonlinear 2D finite-difference analysis of basement retaining walls designed for half the PGA results showed satisfactory performance regarding drift, which revealed that current design practices of basement walls lead to over-conservative design [19]. Similar conclusions were drawn through centrifugal tests [20,21] and shake table tests on RC retaining wall [22], which suggested low seismic earth pressures compared to the corresponding theoretical calculations. Other studies on the seismic behavior of retaining walls considered various parameters, including backfill density, cohesion, pore water pressure, acceleration response, etc. [23–25]. These aspects somewhat contributed to a better framework for understanding the seismic behavior of basement walls.

Past research on seismic behavior of basement retaining walls is reasonable, mainly focusing on centrifugal tests, which lack quantification of seismic parameters and interaction between out-of-plane and in-plane forces. Moreover, previous research on basement walls focuses on monolithic RC walls, and literature is short of experimental studies on precast RC structural walls as basement walls. Underground construction of monolithic RC walls is quite a laborious and time-consuming task, owing to which precast RC panels may be adopted for basement walls in multi-story buildings. To this consideration, the paper attempts to investigate the seismic behavior of a precast RC wall under combined constant out-of-plane and in-plane cyclic loading to obtain the seismic design parameters and implement the system as a basement wall in buildings. A full-scale experimental investigation is carried out, which is validated numerically, and parametric studies conducted to study the effect of wall aspect ratio and backfill density on seismic response of the precast RC wall. Often, basement walls may require large thickness to counteract out-of-plane backfill pressure and buckling. Nevertheless, the adoption of thick precast RC wall panels is undesirable due to their heavy mass, which requires substantial efforts in the transportation and installation process. To this consideration, the proposed precast RC wall system is developed as a double-leaf system, having two outer precast RC panels enclosing a void core for post-erection concreting.

2 Experimental program

2.1 Precast double-leaf system

A full-scale precast RC wall, 3700 mm high and 1250 mm wide with 300 mm thickness, was tested under constant out-of-plane and in-plane cyclic load. The structural wall was designed in compliance to IS 13920: 2016 [26] for 400 kN in-plane lateral load and developed as a precast double-leaf system (PDLS) consisting of two 70 mm thick precast RC panels enclosing 160 mm hollow core, which was later filled with M30 grade in situ concrete. During the fabrication, the internal surface of precast panels was undulated for better bonding of the precast panel with in situ concrete. A 75 mm thick and 150 mm high RC band surrounding the wall, whose reinforcement was projected from the footing, was constructed at the wall base to impart resistance against overturning and sliding of precast RC panels and to disallow the development of cold joint between raft footing and wall. Hollow-core was provided with 8 mm diameter

longitudinal bars, which were embedded into the raft up to twice the development length of the bars. The precast RC panels were connected through three 8ϕ-215 mm long truss connectors or steel lattice girders along the length of the wall, fixed continuously throughout the wall height. Vertical reinforcement was provided as 0.25% steel ratio, whereas 8ϕ@200c/c reinforcement was provided in the horizontal direction, based on the resisting shear. Longitudinal reinforcement required in the wall was critically distributed in hollow core and confining precast panels to fulfill the design requirements of IS 13920: 2016 [26]. Figure 1 illustrates the structural configuration of PDLS.

2.2 Test set-up

The wall was tested under reversed cyclic in-plane lateral loading in quasi-static displacement controlled mode at the top level and simultaneous out-of-plane loading simulated by the backfill sand, with a density of 1632 kg/m^3, and angle of friction as 37°. The wall was erected on a 2425 mm × 1900 mm × 250 mm precast RC footing, adequately fixed to the laboratory floor with 32 mm diameter high strength steel anchors. The backfill sand was confined with two 1815 mm × 3900 mm × 175 mm precast RC walls, installed adjacent to the test wall at both sides, as shown in Fig. 1. Backfill sand from the third side was confined through an already existing RC wall in the laboratory. The set-up allows backfill width to be 1815 mm, which is expected to develop a sufficiently large failure surface as per the findings of Yang and Tang [27]. An 1890 mm × 1050 mm × 200 mm precast RC slab was rested on the walls to simulate actual conditions for basement walls. Figure 2 demonstrates the installation process of PDLS in the laboratory. It shall be noted that the height of the test wall is projected beyond the slab level to apply in-plane lateral load, taking a total height of the wall to 4375 mm. A two-way acting servo-hydraulic programmable actuator with + 75 mm stroke length and 500 kN loading capacity was deployed to apply unidirectional reversed cyclic in-plane load. In-plane lateral load from the actuator was transferred to the wall through steel I-section and 20 mm thick steel plates, which in turn were connected to two 32 mm diameter steel rods on each side of the wall, which transferred the load from one end to the other to simulate cyclic loading condition. Figures 3(a) and 3(b) show the test set-up's schematic diagram, and the actual view, respectively. Linearly Variable Displacement Transducer (LVDTs) for measuring displacements and Fiber Bragg Grating (FBG) sensors for measuring concrete strain were mounted on the wall surface at critical locations, and connected to Data Acquisition Systems for feedback response during the test. Three LVDTs each were placed on both sides of the wall, along the thickness at different levels (Fig. 3) to capture in-plane displacement. Four LVDTs were fixed on the front surface of the wall to measure out-of-plane deformations along the height. A total of 8 FBG sensors were fixed diagonally on the wall surface at different levels. Two FBG sensors each were fixed at the bottom and top of the wall, while two were fixed in the center of the wall in cross-orientation, as shown in Fig. 3. The

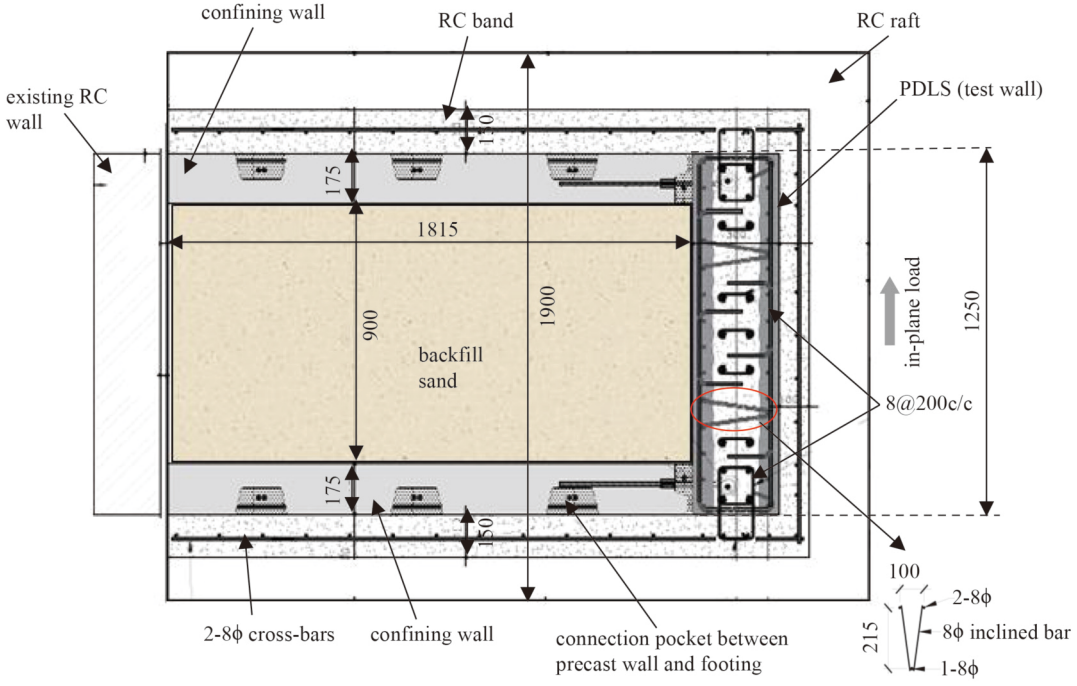

Fig. 1 Structural configuration of PDLS along with test arrangement.

Fig. 2 Installation of PDLS in laboratory.

other two sensors were placed at the height of 1200 m from the base of the wall, designated as middle sensors. Additionally, load cells along the height were placed on the wall's internal surface to capture the backfill load. The displacement time history was drawn as per the loading protocol of ASTM-E-2126 [28]. Accordingly, the wall was subjected to cyclic displacement with increasing amplitudes with every set of amplitude repeating three times, as displayed in Fig. 4. The current loading criterion delivers a frequency of 0.4 Hz, which is suitable for preventing internal effects due to the weight of the wall and loading fixtures during the cyclic test. The test was terminated when the in-plane lateral load dropped to 85% of the peak load, which complies with the energy equivalence criterion, which considers the ultimate state of being at 15%–20% degradation of the maximum load. This ultimate state corresponds to the strength or capacity of an idealized bi-linear system equivalent to a nonlinear capacity curve and is considered the estimate of the ultimate lateral load-carrying capacity of the structural system.

3 Numerical simulation

To validate the experimental findings and conduct parametric studies, numerical simulation of PDLS under combined in-plane and out-of-plane loading was performed using Finite Element Analysis (FEA) in ABAQUS software.

3.1 Modeling approach

An integrative modeling approach is required to predict structural response, such as nonlinearity and damage pattern. With this consideration, Concrete Damage Plasticity (CDP) approach was followed to speculate the structural behavior under tension and compression loading. CDP model is governed by plasticity, based on continuum damage mechanics, scalar damaged elasticity, and a combination of compression plasticity and isotropic tension [29]. Hardening variables govern the yield and failure mechanism under compression and tension action. The tension stiffening model has been adopted to model the concrete behavior in tension due to its brittle nature [30]. Tension stiffening is favorable with regard to the strain softening response of cracked concrete. Plastic strain (ε_t^{pl}) may be evaluated through cracking strain (ε_t^{ck}) as:

$$\varepsilon_t^{pl} = \varepsilon_t^{ck} - \frac{d_t}{(1-d_t)}\frac{\sigma_t}{E_0}, \tag{1}$$

where d_t = plastic strain function; σ_t = stress due to tension; and E_0 = elastic modulus.

Figures 5(a) and 5(b) portray the theoretical stress versus strain plots for uniaxial compression and tension action, respectively. Concrete shows linear uniaxial behavior under compression, defined by hardening of stress till the inception of yield and softening of stress in the plastic phase following the ultimate stress. In tension model, the behavior is linearly elastic till the failure

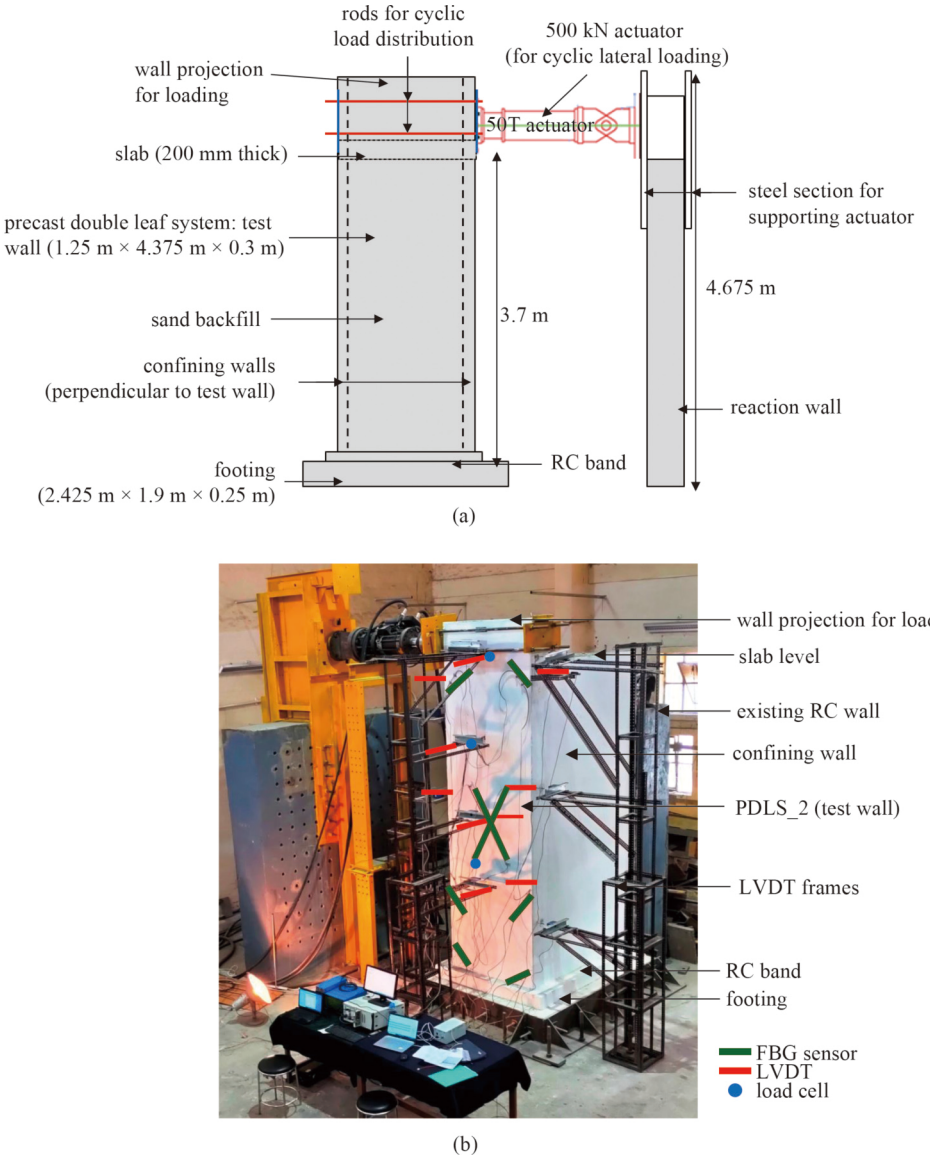

Fig. 3 Test set-up. (a) Schematic diagram; (b) actual view of the test set-up.

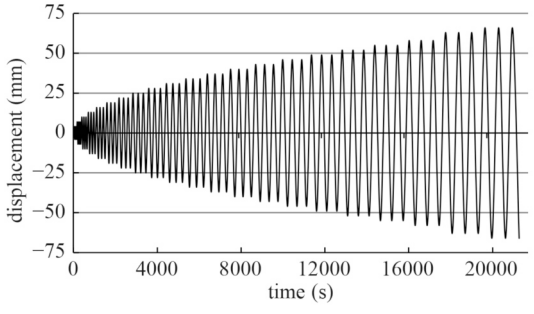

Fig. 4 Cyclic displacement time history.

stress, illustrating the initiation of microcracking in concrete, post which inception of macro-cracks eventuates with strain softening. Table 1 reports material properties and CDP parameters considered for modeling of the wall [31].

3.2 Material and geometrical modeling

The PDLS wall was modeled with similar material and geometrical properties as the tested wall specimen. In situ core, precast panels, raft, and encompassing band were modeled as solid 3D elements, whereas steel rebars and truss elements were modeled as planar wire elements with embedded constraint in the concrete (host element) for adequate connection between the rebar nodes and concrete element. Tie constraint was provided between the rebars in cast-*in situ* element embedded into the footing (raft), which imparts integrity and simulates real conditions for joint modeling. Hexahedral elements were assigned to solid sections and meshed with hourglass control, reduced integration, and 8 noded linear brick elements (C3D8R). Multiple reduced integration elements were assigned across the wall thickness to capture the

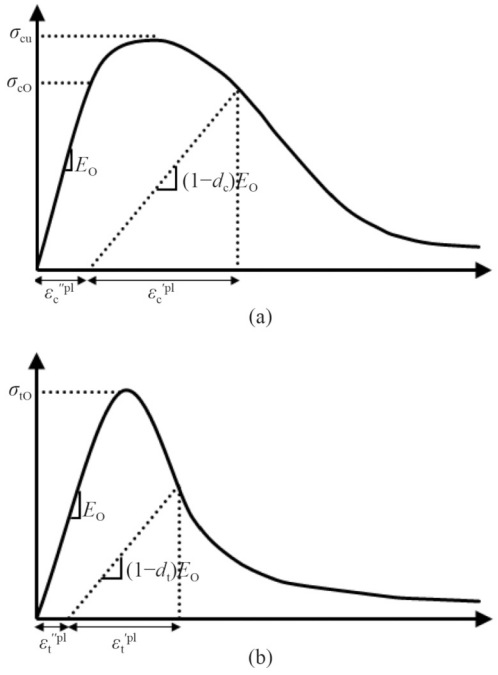

Fig. 5 Response of concrete to uniaxial loading in (a) compression; (b) tension.

Table 1 Material properties and CDP parameters for numerical modeling [31]

property	concrete	steel
density (kN/m^3)	24.0	78.5
Young's modulus (N/mm^2)	29503	2×10^5
Poisson's ratio	0.19	0.29
dilation angle (°)	31	–
eccentricity	0.1	–
f_{bo}/f_{co}	1.16	–
k	0.667	–
viscosity parameter	0	–

flexural response with accuracy. Line elements were assigned to steel rebars and truss elements, which were meshed with 2 noded linear truss elements (T3D2). Raft base was assigned with encastre (fixed) boundary condition, which restrains the element from moving. Elements were meshed according to the thickness to provide proper node-to-node connectivity and avoid mesh distortion. Thus, the wall was meshed into 150 mm × 150 mm elements, which was found to deliver acceptable results from mesh convergence studies. Convergence criteria type included load and displacement checks until the equilibrium is reached within tolerance in terms of default threshold values of ABAQUS. The analysis algorithm is shown in Fig. 6. Static nonlinear analysis was carried out under displacement controlled monotonic load exerted at the top level of the wall as in the experimental study.

4 Results and discussions

The seismic behavior of tested PDLS was studied and analyzed based on the experimental and numerical measurements of damage pattern, in-plane capacity, lateral earth pressure, strain, stiffness degradation, drift, ductility, response reduction or structural behavior factor, dissipation of energy, and damping ratio as discussed below. To facilitate the seismic behavior of the proposed PDLS, different damage states, i.e., elastic (yield) limit, the maximum limit, and ultimate state were considered important performance milestones, for which control points were derived by bi-linear idealization of obtained experimental envelop curve of in-plane load and displacement.

4.1 Damage pattern

The damage commenced with the occurrence of few hairline cracks along the wall thickness, which further

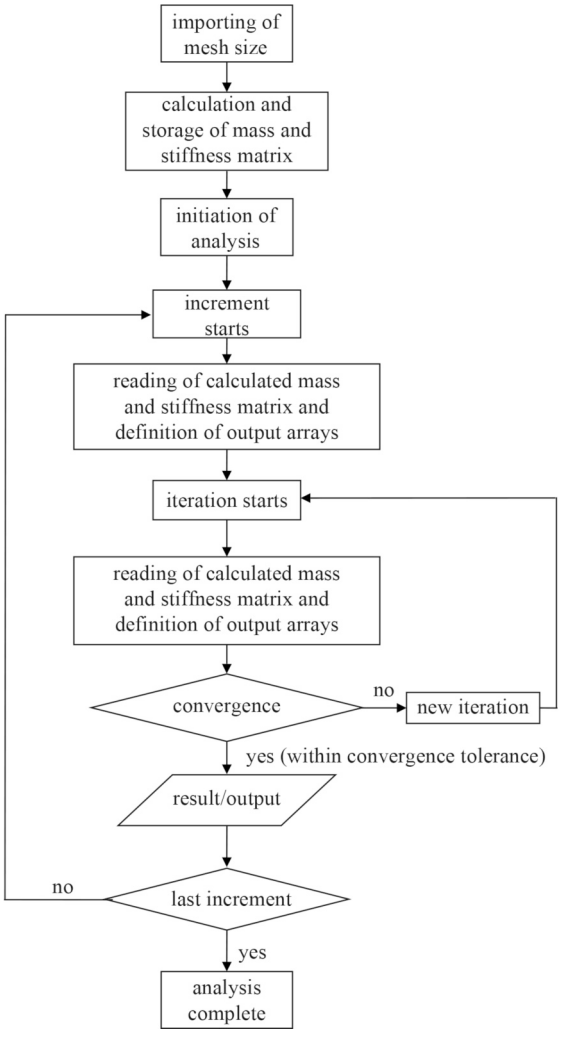

Fig. 6 Analysis algorithm.

increased in numbers and became significant at an in-plane lateral load of approximately 270 kN during the displacement cycle of 15 mm. Separation crack on both sides between the test wall (PDLS) and the confining walls was observed at a cycle of 20 mm. At this point, PDLS tilted in an out-of-plane direction to about 7 mm. This gap continued to increase in further displacement cycles. Several hairline cracks occurred along the wall thickness at 20–25 mm displacement cycle. These cracks expanded and continued to widen in subsequent displacement cycles. The front wall surface did not demonstrate considerable damage till 25 mm deformation at a corresponding in-plane lateral load of 296.6 kN, after which the wall began to experience horizontal cracks near the wall edge at mid-height, which propagated diagonally toward the center of the wall as the test progressed. Further cycles witnessed continuous expansion and widening of cracks on the front surface, increasing concrete strain. Diagonal cracks, starting from the wall edge and propagating inwards, were perceived near the toe region during the displacement cycle of 35 mm. Post maximum resistance, i.e., 303.61 kN at 39 mm displacement, lateral load began to reduce, and existing cracks on the wall surface expanded. Simultaneously, the separation crack between confining walls and PDLS increased, along with the inception of concrete spalling, which was a direct consequence of the widening of existing cracks. Separation crack and flexural cracks on the front surface further advanced in subsequent displacement cycles. During 45–50 mm deformation cycles, several cracks in the left and right boundary regions of the wall were detected and the expansion of existing cracks. By this point, the whole system inclined to about 30 mm in the out-of-plane direction, which resulted in an excessive spillage of backfill sand and indicates an out-of-plane movement of PDLS. Interestingly, no de-bonding occurred between cast-in situ concrete of the core region and precast RC panels, except few minor severance cracks between the two at higher loading, revealing a satisfactory bond between two concrete elements. A strong bond is attributed to the provision of lattice truss girders, which held the precast RC panels together. Undulations on the internal surface of precast panels also contributed to the bond as it bestowed better gripping between *in situ* and precast concrete. Significant spillage of sand from the crack formed between the PDLS and confining walls was observed at 50–55 mm displacement cycles. A crack at the base of the wall was observed, which signified the inception of severance between the precast panel and RC band. It is worthy to note that the encompassing RC band offered resistance against overturning and sliding of precast RC panels, which consequently resulted in separation crack at their interface. Eventually, at concluding cycles, the commencement of concrete crushing at bottom corners of the wall was witnessed, eventuated as a result of induction of tensile and compressive stresses due to continuous push-pull loading. Overall, the damage pattern in PDLS was dominated by flexure, which is a feature of walls having a high aspect ratio. The wall also exhibited considerable out-of-plane movement due to lateral pressure from the backfill. This shows out-of-plane instability, which has the potential of sudden collapse under the continuous imposition of in-plane load. However, despite the wall being fixed at the bottom and top, it did not suffer from out-of-plane buckling at the center, which is attributed to the large thickness of the wall, thereby imparting high stiffness and resistance against buckling. The numerical model showed a similar damage pattern, depicting maximum damage near the wall edge with reducing intensity toward the central region of the wall, accompanied with damage at the bottom corner, indicating concrete crushing. Figure 7 depicts the damage pattern of PDLS, showing out-of-plane deflection, damage on wall surface, and comparison with numerical observations.

4.2 Strain

The maximum strain in concrete was determined to be 3133 μm/m near the boundary regions, about one-third distance from the wall base, coinciding with the region of maximum cracks. As expected, sensors placed near the top of the wall showed insignificant strain owing to the absence of damage in the top region. Strain in the bottom region of the wall increased rapidly up to 440 μm/m till the elastic limit compared to strains in other regions, which showed a minor increase up to 65–70 μm/m in top and center regions and 111 μm/m in the middle region. This might be due to the induction of stresses in the bottom corners. However, as the test progressed, middle regions developed flexural cracks, resulting in excessive strains surpassing that in the bottom. The tested wall exhibited strain-softening behavior after attaining the peak load, as can be observed from Fig. 8, wherein all the sensors demonstrated a gentle declining sloped curve between the load and strain, indicating strain softening. This is the direct consequence of material strength deterioration due to the brittle nature of concrete. Strain response of the tested wall was monitored during the entire test and plotted for the in-plane load in Fig. 8.

4.3 In-plane capacity

The in-plane capacity of a wall is its ability to withstand the in-plane lateral (seismic) load without failure or significant damage. Figure 9(a) portrays the average in-plane capacity-displacement hysteresis and envelop curve of all the cyclic displacements in push-pull directions for PDLS. While Fig. 9(b) shows the in-plane capacity-

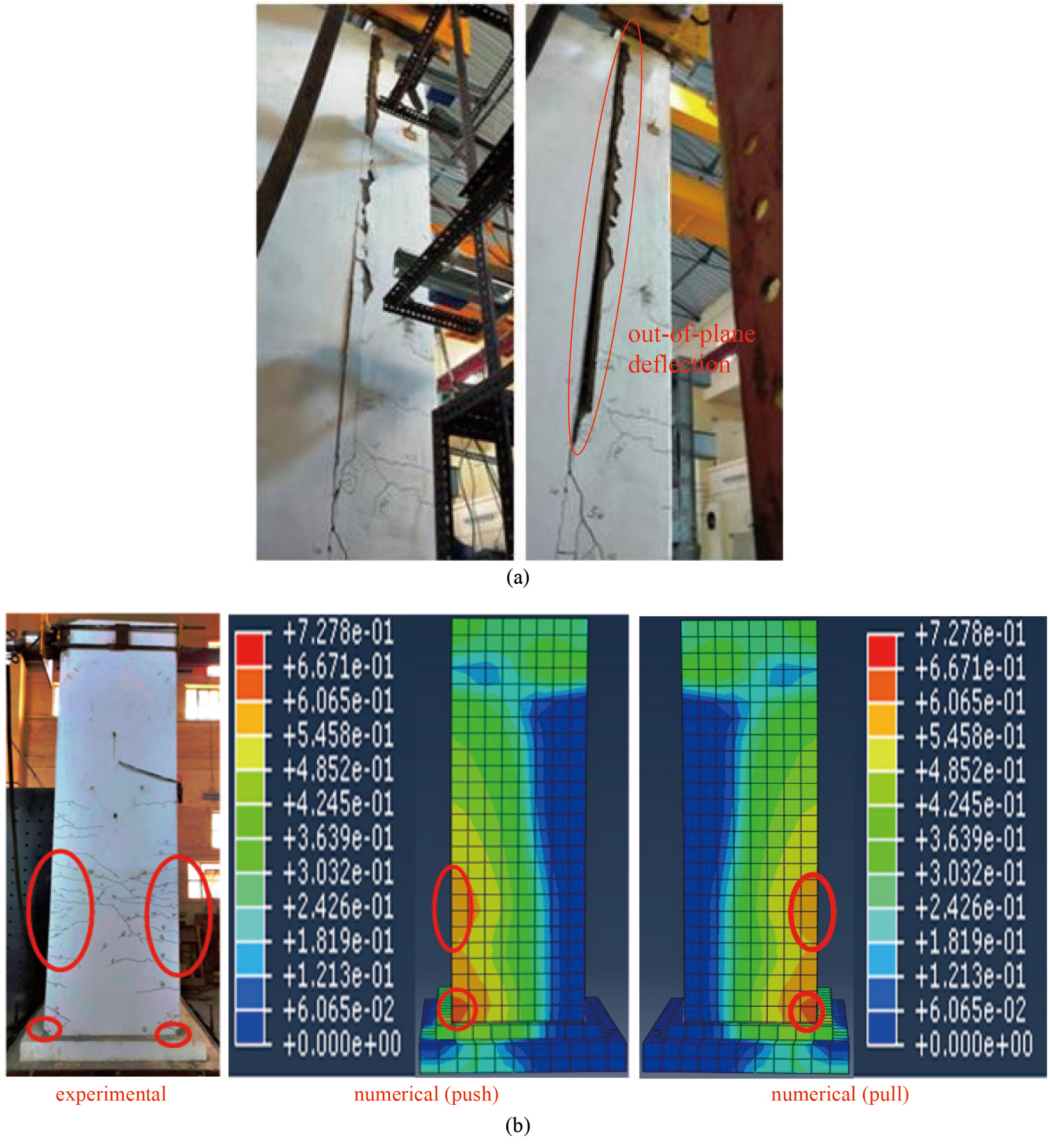

Fig. 7 Damage pattern of PDLS: (a) damage along the thickness and inclination in out-of-plane direction; (b) comparison of experimental and numerical (tension) damage.

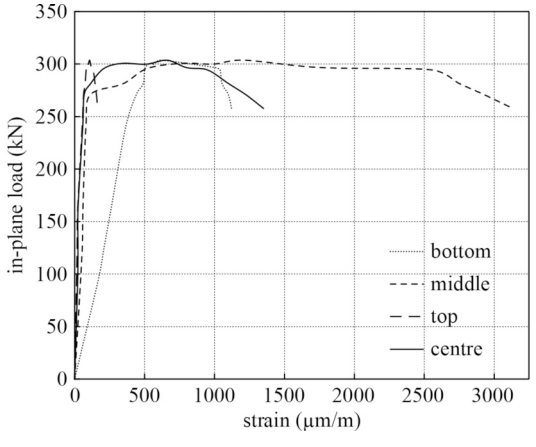

Fig. 8 Variation of concrete strain with in-plane load.

displacement envelop curves from experimental and numerical analysis. The PDLS demonstrated linear behavior until the first considerable crack at an in-plane lateral load of 270.82 kN and displacement of 12.32 mm. The yield point from numerical FEA was determined at 264.00 kN at 13.85 mm lateral deformation. Linear behavior was identified with lean and slender hysteresis loops indicating small energy dissipation. PDLS attained a maximum in-plane capacity of 303.61 kN in the push cycle, whereas 286.05 kN in the pull cycle, during the displacement cycle of 40 mm. The corresponding values from the numerical analysis were determined to be 322.60 kN at 37.34 mm lateral displacement. Post peak resistance, the wall began to behave in a nonlinear manner. With the continuous displacement, load began to degrade untill the test wall gained an ultimate in-plane

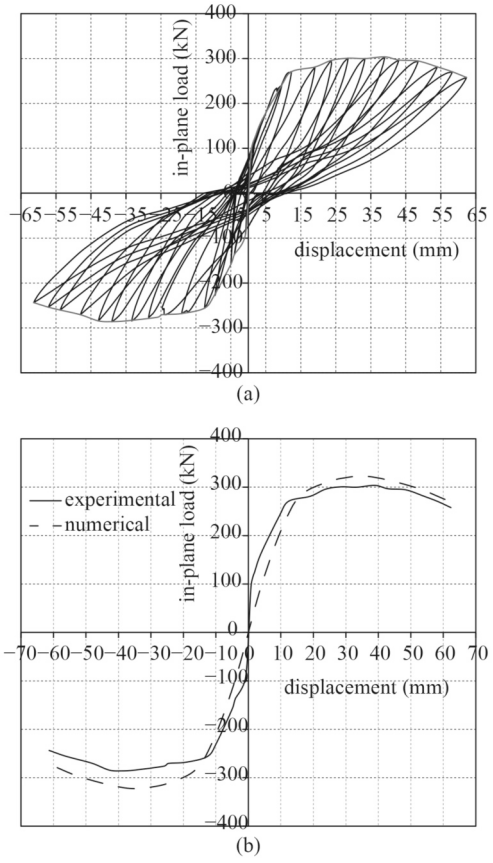

Fig. 9 In-plane load versus displacement curve for tested wall: (a) hysteretic curve; (b) experimental and numerical envelop curves.

capacity of 257.76 kN at 62.36 mm deformation, while the numerical model exhibited an ultimate limit at 60.5 mm displacement with load degradation at 274.75 kN. The tested wall could not reach its design load capacity of 400 kN due to out-of-plane pressure generated from the backfill. Table 2 presents the in-plane capacity and deformation at different limit states of the tested PDLS wall.

4.4 Lateral earth pressure

Backfill sand exerted a constant out-of-plane load to the wall. The sand was at rest at the inception of the cyclic loading, which tend to move toward the wall, generating a state of active pressure on the wall. This may be inferred from the fact that the wall moved in an out-of-plane direction during the test, as observed from visual observations. Theoretical backfill pressure is computed from Rankine's earth pressure theory as:

$$P_{\text{th}} = \frac{1}{2} K_{\text{a}} \gamma H^2, \tag{2}$$

where P_{th} = theoretical backfill pressure; K_{a} = coefficient of active earth pressure; γ = backfill density; and H = height of the wall. It was recognized that the theoretical out-of-plane load as obtained from Rankine's theory is considerably higher than the experimental observations, which mirror the observations from other approaches, such as MO method as reported in Refs. [17,18]. Figure 10 shows the experimental and theoretical out-of-plane load with respect to the wall height.

Table 2 Seismic parameters for PDLS

seismic parameter	limit	experimental			numerical
		push	pull	average	
in-plane capacity (kN)	crack	240.56	227.54	234.05	227.90
	yield	270.82	256.50	263.66	264.00
	maximum	303.61	286.05	294.83	322.60
	ultimate	257.76	243.79	250.78	274.75
displacement (mm)	crack	9.53	9.75	9.64	11.17
	yield	12.32	12.52	12.42	13.85
	maximum	39.00	39.00	39.00	37.34
	ultimate	62.36	61.35	61.86	60.50
stiffness (kN/mm)	crack	25.24	23.33	24.28	20.40
	yield	21.98	20.49	21.23	19.06
	maximum	7.78	7.33	7.56	8.63
	ultimate	4.13	3.97	4.05	4.54
drift (%)	crack	0.26	0.26	0.26	0.30
	yield	0.33	0.33	0.33	0.37
	maximum	1.05	1.05	1.05	1.01
	ultimate	1.68	1.66	1.67	1.64
damage index	crack	0	0	0	0
	yield	0	0	0	0
	maximum	0.66	0.64	0.65	0.55
	ultimate	0.81	0.81	0.81	0.76
ductility	–	5.06	4.90	4.98	4.37
structural behavior factor	–	4.86	4.57	4.72	4.89
ductility class					
ASCE 41-17	–	high			high
EN 1998-1: 2004	–	moderate to high			moderate to high

4.5 Stiffness degradation

A weighted average of stiffness in both pull and push loading is computed as the ratio of in-plane load ($P_{\pm i}$) to the corresponding displacement ($d_{\pm i}$) during + ith cycle, i.e., push and –ith, i.e., pull loading and is given as:

$$K_i = \frac{|P_{+i}| + |P_{-i}|}{|d_{+i}| + |d_{-i}|}. \tag{3}$$

Stiffness is designated by the degree of damage

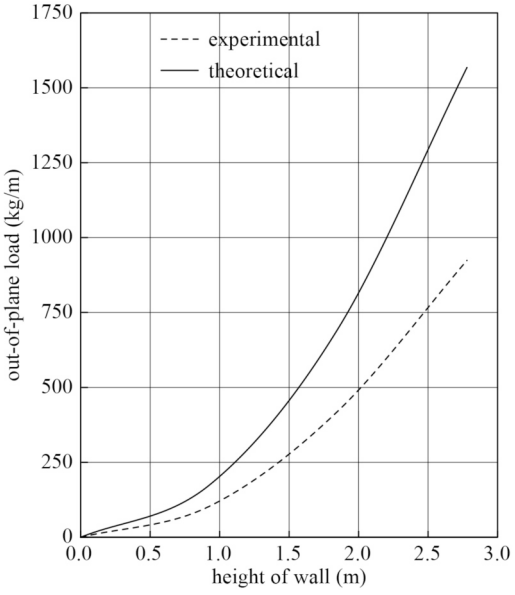

Fig. 10 Out-of-plane load with respect to wall height.

undergone by the wall during the test. Initial stiffness (K_{in}) of the wall was evaluated at the initiation of the cyclic test. Yield or elastic stiffness, which is effective stiffness (K_{cr}), was calculated at the occurrence of significant cracks. Likewise, stiffness was also determined at the maximum lateral load (K_{max}) and ultimate state (K_u) to characterize its behavior at various limit states. K_{in} was determined to be 116.98 kN/mm, which declined to 21.98 kN/mm at the elastic limit. Rapid fall in stiffness was perceived during the inceptive cycles, which afterward exhibited gentle degradation. The steep behavior of stiffness degradation is due to flexural cracks on the wall. Figure 11 lists the stiffness degradation with reference to the normalized stiffness with drift and damage index for PDLS. Quantification of damage index is carried out according to Carrillo [32] as described in Section 4.7. Table 2 gives the stiffness obtained at various limit states of the tested wall.

4.6 Deformation characteristics

Drift, ductility, and structural behavior factor were quantified to study the deformation characteristics of the tested wall. The drift (Θ) is computed at different limit states, i.e., yield or elastic limit, maximum resistance, and ultimate limit. To study the deflection profile of wall at different states, drift is expressed graphically along the height at each damage state. Figure 12 presents the deformation profile of PDLS at different limit states. Ultimate drift was found to be 1.69% and 1.66% in the push and pull directions, respectively. While ultimate drift from the numerical analysis was found to be 1.64%, ductility (μ) can be expressed as the ratio of displacement at the ultimate state ($d_{\pm u}$) to the displacement at the elastic state ($d_{\pm e}$). It is given as:

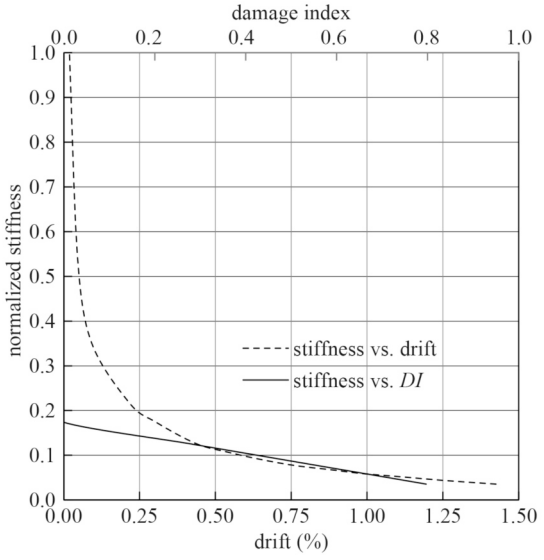

Fig. 11 Stiffness degradation with damage index and drift.

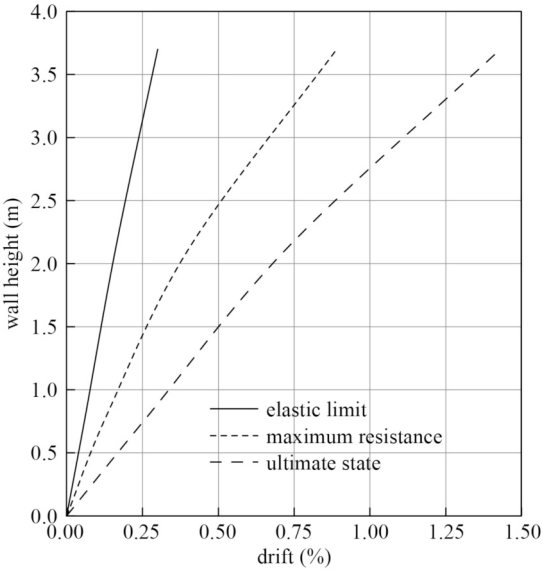

Fig. 12 Drift against height of the wall.

$$\mu = \frac{|d_{+u}| + |d_{-u}|}{|d_{+e}| + |d_{-e}|}. \quad (4)$$

The wall achieved an ultimate displacement of 62.36 mm during the experimental investigation at 85% of the maximum load, which corresponds to ductility of 5.06. The numerical study showed a ductility of 4.37, which is well comparable with the experimental finding. ASCE-41-17 [33] acknowledges structural components with calculated displacement ductility of more than 4 to have high ductility demand. Remarkable ductility is credited to the non-failure of wall-footing connection, which eventually provided tensile resistance after attaining an elastic state and enable the wall to achieve more displacement.

Response reduction or structural behavior factor represents the ability of the structural system to dissipate energy through nonlinear behavior. This factor is adopted to evaluate design shear by normalization of linear elastic seismic force for an ideal linear elastic structural system. Structural behavior factor (q), which may be evaluated as:

$$q = \frac{P_{e,max}}{P_{ude}}, \tag{5}$$

where $P_{e,max}$ = seismic load in a completely elastic structural system; and P_{ude} = ultimate design seismic load. Structural behavior factor was determined as 4.86 and 4.57 for push and pull directions, respectively. The numerical analysis demonstrated the same to be 4.89. It is to be noted that the structural behavior factor for RC wall according to EN 1998 (Part 1): 2004 [34] can be considered as 3.0 and 4.0 for medium and high ductile walls, respectively. Thus, the proposed structural wall may qualify for a medium to high ductility wall. Table 2 presents the deformation characteristics of tested PDLS.

4.7 Damage index

Damage index (DI) is indicative of structural damage occurred and its performance level under the applied loading, which may be quantified as:

$$DI = 1 - \frac{K}{K_{cr}}, \tag{6}$$

where K = stiffness at the state where the DI is computed, and K_{cr} = yield or elastic stiffness. The damage initiated at 270 kN in-plane load as slight physical damage. Substantial damage was speculated at the ultimate state. The same was characterized with the determination of DI at the ultimate limit state, which was found to be 0.81, indicating severe damage. This may be due to the excessive flexural cracks and concrete crushing at the bottom corners, which lead to loss of stiffness at the ultimate limit state. Still, the PDLS did not exhibit the 'potential for collapse' even at the ultimate limit state, according to the performance indicator of Carrillo [32]. Table 3 summarizes the DI obtained from experimental results and corresponding performance levels.

4.8 Energy dissipation

Cumulative input energy can be given as the amount of work done to move the test wall from test initiation to the ultimate state. The cumulative input energy is the area confined under the hysteretic loops, whereas the area confined within the hysteresis loop corresponds to cumulative dissipated energy. PDLS exhibited remarkable energy dissipation of 70.05% in the push and 65.8% in the pull direction at the ultimate limit state, which may be credited to its ductile behavior during the post-peak stage. Table 4 summarizes the cumulative input and dissipated energy determined at different limit states for the tested wall. Figure 13 shows the curves of cumulative input and dissipated energy with respect to the drift and damage index. Figure 14 gives the plot of energy ratio against the wall drift. It can be interpreted from the plot that the energy ratio increased till the peak load, after that stablizing till the ultimate limit state.

4.9 Equivalent viscous damping

The equivalent viscous damping coefficient (ε_{eq}) is a function of energy dissipated in a particular cycle and elastic energy accumulated in an equivalent linear elastic structure. It may be evaluated as [35]:

$$\varepsilon_{eq} = \frac{E}{2\pi dP}, \tag{7}$$

where E = energy dissipated in the particular cycle; d = displacement at the particular cycle; and P = in-plane

Table 3 Damage index at different limit states

limit state	damage index	damage level as per Carrillo [32]	performance level as per Carrillo [32]	damage observed
crack limit	0	no damage	immediate occupancy (IO)	insignificant hairline cracks
elastic limit	0	minor damage	immediate occupancy (IO)	minor cracks on wall surface
maximum resistance	0.65	moderate to significant damage	collapse prevention (CP)	widening of existing cracks, inception of concrete spalling
ultimate state	0.81	severe damage	–	concrete crushing at bottom corners of the wall, significant out-of-plane deflection

Table 4 Energy parameters at different states for tested wall

limit state	push		pull		average		ratio (%)
	input (kN·mm)	dissipated (kN·mm)	input (kN·mm)	dissipated (kN·mm)	input (kN·mm)	dissipated (kN·mm)	
elastic limit	1543	632	1385	756	1464	694	47.78
maximum resistance	10008	6688	9326	5845	9667	6266	64.75
ultimate state	16673	11679	15580	10260	16127	10969	68.00

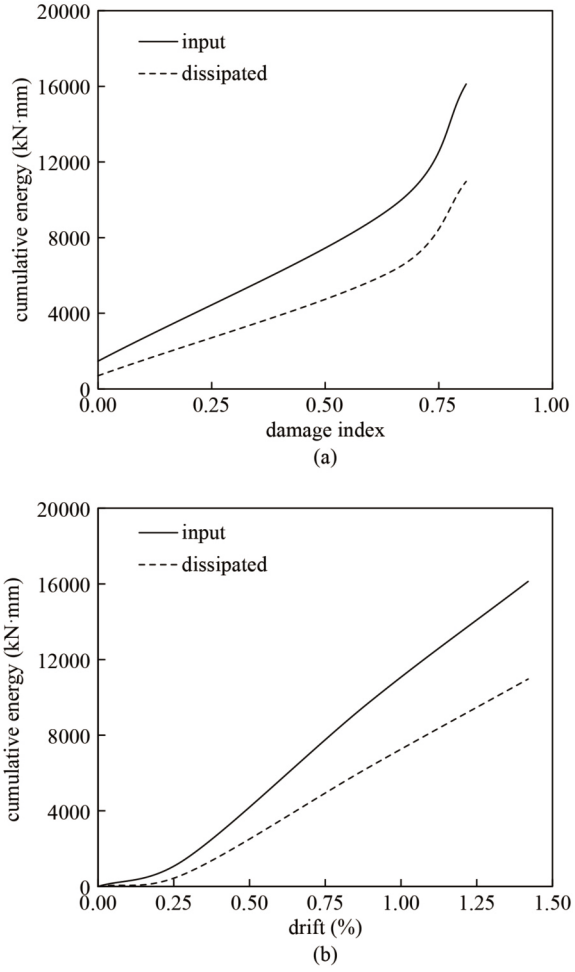

Fig. 13 Cumulative input and dissipated energy against (a) damage index; (b) drift for the tested wall.

capacity at the particular cycle. The equivalent damping ratio of the tested wall was computed at different states, which is expressed graphically with respect to the drift of the tested wall (Fig. 14). It is interpreted from the curve that the equivalent damping ratio reaches up to 11.66% as the displacement increases from the beginning till the ultimate state.

5 Parametric studies

Since a single experiment was performed on a particular

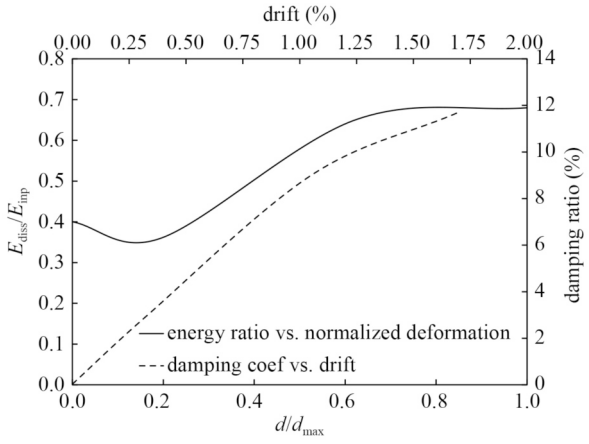

Fig. 14 Energy and equivalent viscous damping ratio against drift.

set of parameters, multiple numerical simulations were carried out to perform parametric studies to evaluate the influence of backfill density and aspect ratio on the out-of-plane behavior of PDLS. The numerical analysis simulating experimental investigation was conducted, along with the models with varying backfill density in the range of 1200 to 1950 kg/m^3, reflecting actual conditions. Additionally, four more sets of the numerical studies were carried out on the wall with lower aspect ratios to study the behavior of intermediate and squat walls. Five cases of aspect ratios are considered, one reflecting experimental specimen (slender), two with reduced length representing intermediate walls, and the other two based on length and height of basement walls commonly found in practice. Table 5 illustrates the configuration of numerical models.

5.1 Effect of backfill density

In-plane capacity and stiffness of the wall are reduced with the increase in backfill density. Nevertheless, deformation characteristics of the wall were found to be independent of backfill density as no significant change in drift and ductility was found with the varying density. The pattern was similar in walls with all the aspect ratios. It can be noted that none of the walls reached their design capacity at yield limit due to lateral earth pressure. Nevertheless, all the squat walls except the one with 1950 kg/m^3 backfill density and intermediate walls till

Table 5 Configuration of numerical models

wall dimensions $L \times H$ (mm)	aspect ratio (classification)	in-plane design capacity (kN)	backfill density (kg/m^3)
1250 × 3700	2.96 (slender)	400	1200, 1350, 1500, 1632, 1800, 1950
1250 × 2500	2.00 (intermediate)	400	1200, 1350, 1500, 1632, 1800, 1950
1250 × 1250	1.00 (intermediate)	400	1200, 1350, 1500, 1632, 1800, 1950
3000 × 2500	0.83 (squat)	800	1200, 1350, 1500, 1632, 1800, 1950
5000 × 2500	0.50 (squat)	800	1200, 1350, 1500, 1632, 1800, 1950

1350 kg/m^3 backfill density surpassed their in-plane design capacity at the maximum limit. Slender walls did not attain their design load, even with low-density backfill. In-plane load versus drift curves for varying aspect ratios of the wall with different backfill densities (γ) are plotted in Fig. 15.

5.2 Effect of aspect ratio

The in-plane load carrying capacity and drift of the walls are affected by the wall's aspect ratio and length. Lower aspect ratio walls demonstrated better performance with the standpoint of the wall's in-plane load-carrying capacity, as expected. The in-plane capacity of the wall was enhanced in the range of 10%–15%, while the in-plane drift reduced by 15% when the aspect ratio is reduced from 2.96 to 2.0 to 1.0. However, walls with an aspect ratio of 1.0 and 0.5 did not demonstrate significant variation in the drift due to an increase in length of the latter. Although, the in-plane capacity of the wall with an aspect ratio of 0.5 is significantly higher due to higher length and lower aspect ratio compared to that with an aspect ratio of 1.0. A similar trend was observed amidst the walls with an aspect ratio of 2.0 and 0.83.

5.3 Relation between in-plane yield and design capacity

Here, the in-plane yield capacity of the basement wall is the lateral load attained up to which the wall remains in the elastic state without experiencing significant damage during the test. While the in-plane design capacity of the wall is the lateral load for which the basement wall is designed, without considering the effect of out-of-plane backfill pressure. It is evident from Fig. 15 that the aspect ratio of the wall plays a vital role in establishing the relationship between in-plane design capacity (V_d) and actual in-plane yield capacity (V_a). The actual in-plane yield capacities of the analyzed walls were normalized with their in-plane design capacities and plotted for the backfill densities for different aspect ratios (Fig. 16). It can be noted that the ratio of V_a and V_d decreased with the increase in backfill density in all five cases of aspect ratios. Thus, the actual in-plane yield capacity of the basement wall is more sensitive to higher backfill densities. A Slender wall (aspect ratio of 2.96) attained V_a equal to $0.73V_d$ at 1200 kg/m^3 backfill density, which showed almost linear behavior till 1950 kg/m^3 backfill density with V_a/V_d as 0.58. A similar pattern was observed for intermediate and squat walls, although the value of V_a/V_d was higher, as can be seen from curves plotted in Fig. 16. The curves may be adopted to speculate the in-plane capacity of the proposed precast RC wall system with different aspect ratios, based on their design load for varying backfill densities.

6 Conclusions

To contribute to enhancing the knowledge about the performance of precast basement walls under combined constant out-of-plane, and in-plane cyclic loading, an experimental and numerical research program was conducted. The wall was subjected to the in-plane lateral load in displacement control mode under a quasi-static state with simultaneous out-of-plane loading. Chief conclusions derived from careful interpretation of experimental and numerical findings are summarized as follows.

1) The tested wall exhibited flexural cracks, owing to a high aspect ratio. The PDLS also exhibited considerable out-of-plane movement due to lateral pressure from the backfill. This shows out-of-plane instability, which has the potential of sudden collapse under the continuous imposition of in-plane lateral load. However, despite the wall being fixed from bottom and top, it did not suffer from out-of-plane buckling at the center, which is attributed to the large thickness of the wall, thereby imparting high stiffness and resistance against out-of-plane buckling. The PDLS did not demonstrate any evidence of detachment or debonding between precast and cast-in situ concrete as steel lattice truss effectively held the precast panels in their position.

2) Seismic parameters determined from the experimental investigation were in good agreement with the numerical studies. The PDLS performed satisfactorily by demonstrating remarkable seismic parameters, thus upraising confidence to accept PDLS basement wall as a substitution of prevalent cast-in situ monolithic RC walls.

3) PDLS delivered superior deformation characteristics governed by their ductile response in the nonlinear phase during the test with smaller residual drift. The PDLS categorizes under 'moderate to highly' ductile wall as per EN 1998 (part 1): 2004, while ASCE 41-17 qualifies such walls for high ductility demand. Substantial deformation characteristics lead to enhanced energy dissipation capacity of the PDLS.

4) In-plane capacity was found to be inversely proportional to the backfill density, while drift, ductility, and structural behavior factor of basement walls were unaffected by the increase in backfill density.

5) Reduction in in-plane capacity was observed with the increasing aspect ratio. Consequently, the ratio of in-plane yield capacity and in-plane design capacity is much affected with the aspect ratio, with all the squat walls attaining in-plane capacity more than 0.7 times its design capacity, while the corresponding ratio for intermediate and slender wall was 0.68 and 0.58, respectively. The V_a/V_u versus backfill density curves may be adopted to predict the in-plane yield load of the basement wall depending on its design capacity, aspect ratio, and backfill density.

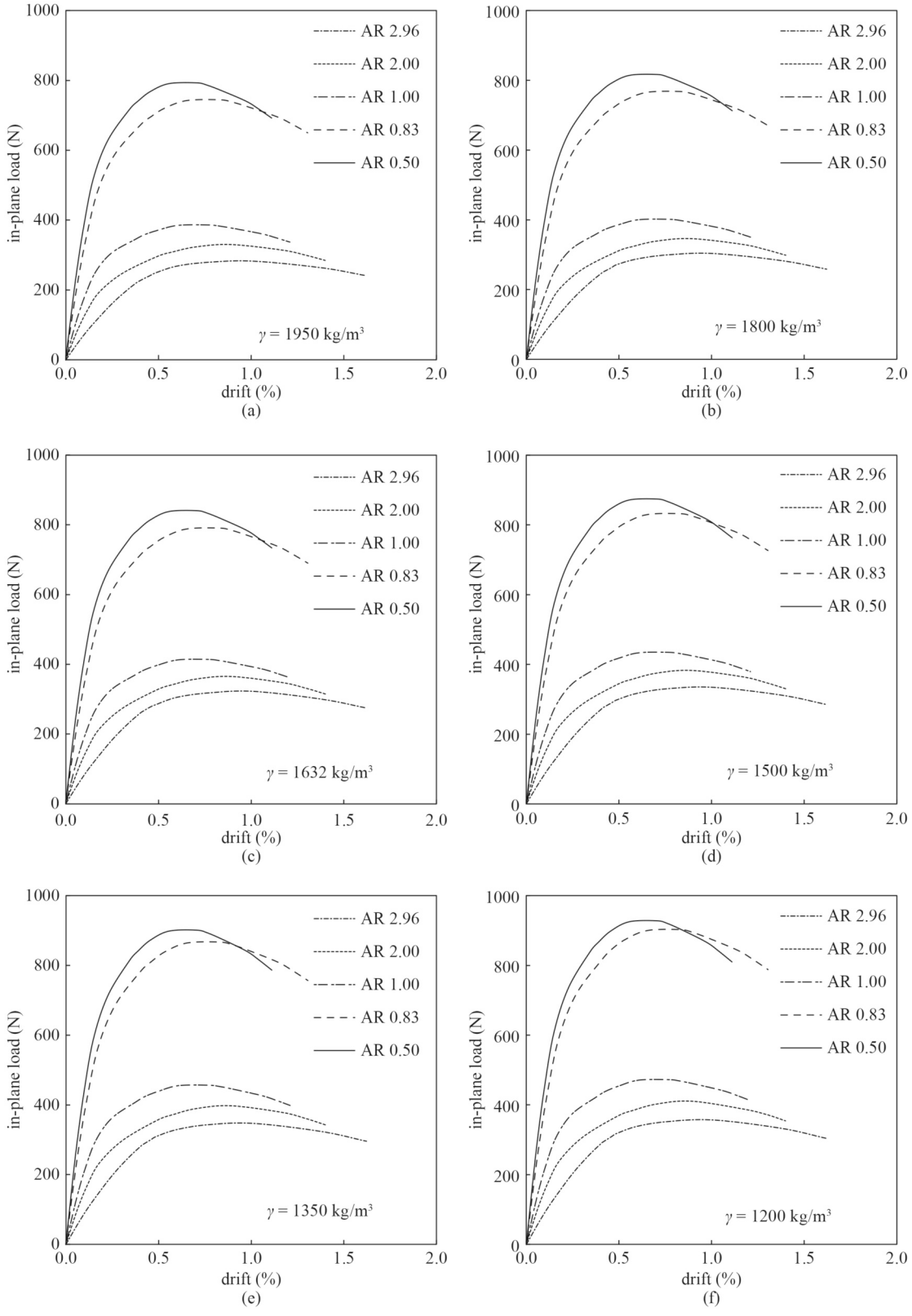

Fig. 15 In-plane load versus drift for varying aspect ratios of wall. (a) γ =1950 kg/m^3; (b) γ =1800 kg/m^3; (c) γ =1632 kg/m^3; (d) γ =1500 kg/m^3; (e) γ =1350 kg/m^3; (f) γ =1200 kg/m^3.

The study concluded that the proposed precast RC structural wall system sustains adequate seismic characteristics as demonstrated through experimental and numerical investigations, along with benefits of efficient

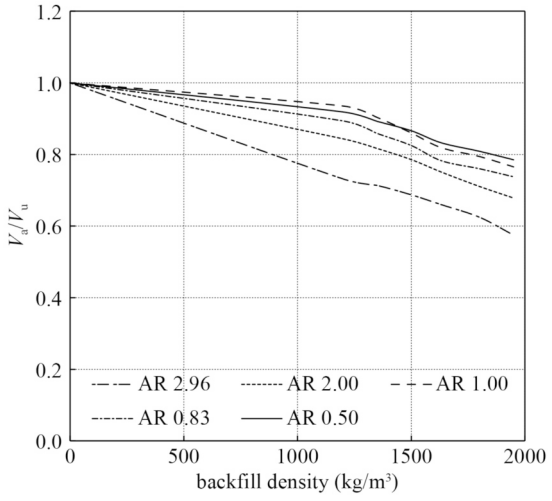

Fig. 16 Ratio of in-plane yield to design capacity of PDLS with varying backfill densities.

and rapid construction methodology, imparting quality and safety in construction. The research program and the advantages of precast technology form the basis to promote PDLS against prevalent cast-in situ monolithic basement walls.

Acknowledgements Authors are grateful to the Director, CSIR-Central Building Research Institute, Roorkee, India for all the support and encouragement during the research work and permitting to publish the paper.

References

1. Singhal S, Chourasia A, Chellappa S, Parashar J. Precast reinforced concrete shear walls: State of the art review. Structural Concrete, 2019, 20(3): 886−898
2. Chourasia A, Singhal S, Parashar J. Seismic performance of prefab RC shear walls: A review. In: Proceedings of CISHR. Srinagar: National Institute of Technology Uttarakhand, 2017, 202−213
3. Brunesi E, Peloso S, Pinho R, Nascimbene R. Cyclic tensile testing of a three-way panel connection for precast wall-slab-wall structures. Structural Concrete, 2019, 20(4): 1307−1315
4. Brunesi E, Peloso S, Pinho R, Nascimbene R. Shake-table testing of a full-scale two-story precast wall-slab-wall structure. Earthquake Spectra, 2019, 35(4): 1583−1609
5. Brunesi E, Nascimbene R, Peloso S. Evaluation of the seismic response of precast wall connections: Experimental observations and numerical modeling. Journal of Earthquake Engineering, 2020, 24(7): 1057−1082
6. Singhal S, Chourasia A, Parashar J. Anchorage behaviour of headed bars as connection system for precast reinforced concrete structural components. Structures, 2020, 27: 1405−1418
7. Singhal S, Chourasia A, Kajale Y, Singh D. Behaviour of precast reinforced concrete structural wall systems subjected to in-plane lateral loading. Engineering Structures, 2021, 241: 112474
8. Jünemann R, de La Llera J C, Hube M A, Cifuentes L A, Kausel E. A statistical analysis of reinforced concrete wall buildings damaged during the 2010, Chile earthquake. Engineering Structures, 2015, 82: 168−185
9. Wood J H. Earthquake-induced soil pressures on structures. Dissertation for the Doctoral Degree. California: California Institute of Technology, 1973
10. Steedman R S, Zeng X. The seismic response of waterfront retaining walls. In: Proceedings of the ASCE specialty conference on design and performance of earth retaining structures. New York: Special Technical Publication 25, 1990, 872−886
11. Veletsos A S, Younan A H. Dynamic response of cantilever retaining walls. Journal of Geotechnical and Geoenvironmental Engineering, 1997, 123(2): 161−172
12. Younan A H, Veletsos A S. Dynamic response of flexible retaining walls. Earthquake Engineering & Structural Dynamics, 2000, 29(12): 1815−1844
13. Mansour M F, Abdel Motaal M A, Elsaba A A. Seismic response of basement walls as partially-yielding retaining walls. Ain Shams Engineering Journal, 2021, 12(1): 181−193
14. Kalasin T, Wood D M. Seismic analysis of retaining walls within plasticity framework. In: Proceedings of the 14th WCEE. Beijing: China Earthquake Administration, 2008, 12−17
15. Kim Y Y, Yoon M S, Han S J, Kim S S. Behavior analysis of reinforced soil retaining wall under cyclic loading. In: Proceedings of the 4th Asian Regional Conference on Geosynthetics. Shanghai: Springer, 2008, 639−644
16. Jia L, He S, Li N, Wang W, Yao K. Stability of reinforced retaining wall under seismic loads. Applied Sciences (Basel, Switzerland), 2019, 9(11): 2175
17. Whitman R V. Seismic design of earth retaining structures. In: Proceedings of the 2nd international conference on recent advances in geotechnical earthquake engineering and soil dynamics. Missouri: ASCE, 1991, 1767−1778
18. Taiebat M, Ahmadnia A, Finn W D L, Ventura C E, Naesgaard E, Devall R H. Seismic assessment of basement walls for different design criteria. In: Proceedings of the 14th Pan-am Conference on Soil Mechanics and Geotechnical Engineering, 64th Canadian Geotechnical Conference. Toronto: Canadian Geotechnical Society, 2011, 1069
19. Amirzehni E, Taiebat M, Finn W D L, DeVall R H. Seismic Performance of Deep Basement Walls. In: Proceedings of the 6th International Conference on Earthquake Geotechnical Engineering. Christchurch: International Society for Soil Mechanics and Geotechnical Engineering, 2015
20. Sitar N, Mikola R G, Candia G. Seismically induced lateral earth pressures on retaining structures and basement walls. In: GeoCongress 2012—Keynote lecture. California: ASCE, 2012, 335−358
21. Candia G, Mikola R G, Sitar N. Seismic response of retaining walls with cohesive backfill: Centrifuge model studies. Soil Dynamics and Earthquake Engineering, 2016, 90: 411−419
22. Zhu H W, Yao L K, Li J. Influence factors on the seismic behavior and deformation modes of gravity retaining walls. Journal of Mountain Science, 2019, 16(1): 168−178
23. Osouli A, Zamiran S. The effect of backfill cohesion on seismic

response of cantilever retaining walls using fully dynamic analysis. Computers and Geotechnics, 2017, 89: 143−152

24. Sharma M. Seismic response of reduced scale soil retaining wall at varying backfill density. Dissertation for the Doctoral Degree. Patiala: Thapar Institute of Engineering and Technology, 2019
25. Konai S, Sengupta A, Deb K. Seismic behavior of cantilever wall embedded in dry and saturated sand. Frontiers of Structural and Civil Engineering, 2020, 14(3): 690−705
26. IS 13920: 2016. Ductile Design and Detailing of Reinforced Concrete Structures Subjected Seismic Forces—Code of Practice. New Delhi: Bureau of Indian Standards, 2016
27. Yang M, Tang X. Rigid retaining walls with narrow cohesionless backfills under various wall movement modes. International Journal of Geomechanics, 2017, 17(11): 04017098
28. ASTM. Standard Test Methods for Cyclic (reversed) Load Test for Shear Resistance of Vertical Elements of the Lateral Force Resisting Systems for Buildings. West Conshohocken, PA: American Society for Testing and Materials, 2009
29. Lubliner J, Oliver J, Oller S, Oñate E. A plastic-damage model for concrete. International Journal of Solids and Structures, 1989, 25(3): 299−326
30. Nayal R, Rasheed H A. Tension stiffening model for concrete beams reinforced with steel and FRP bars. Journal of Materials in Civil Engineering, 2006, 18(6): 831−841
31. Goh W I, Mohamad N, Abdullah R, Samad A A A. Finite element analysis of precast lightweight foamed concrete sandwich panel subjected to axial compression. Journal of Computer Science and Computational Mathematics, 2016, 6(1): 1−9
32. Carrillo J. Damage index based on stiffness degradation of low-rise RC walls. Earthquake Engineering & Structural Dynamics, 2015, 44(6): 831−848
33. ASCE-41-17. Seismic Evaluation and Retrofit of Existing Buildings. Virginia: American Society of Civil Engineers, 2017
34. Code P. Eurocode 8: Design of Structures for Earthquake Resistance—Part 1: General Rules, Seismic Actions and Rules for Buildings. Brussels: European Committee for Standardization, 2004
35. Rodrigues H, Varum H, Arêde A, Costa A. A comparative analysis of energy dissipation and equivalent viscous damping of RC columns subjected to uniaxial and biaxial loading. Engineering Structures, 2012, 35: 149−164